DOI: 10.1002/ente.201402074

An Efficient Photoelectrochemical Hydrogen Evolution System using Silicon Nanomaterials with Ultra-High Aspect Ratios

Duck Hyun Lee,*[a] Sai P. R. Kobaku,[b] Young-Rae Hong,[c] and Jae Young Kwon[a]

We fabricated ultra-high aspect ratio silicon nanomaterials, including a silicon nanomesh and silicon nanowire array, on a wafer scale for efficient photoelectrochemical hydrogen production. These silicon nanomaterials (feature size $\approx$20 nm) possess a high aspect ratio to increase the optical absorptivity of the cells to approximately 95% over a broad range of wavelengths. The silicon nanomesh and Si nanowire cells achieved high photocurrent values of 13 and 28 mA cm^{-2}, respectively, which are increased by 200% and 570% in comparison to their bulk counterparts. In addition, these scalable Si nanomaterials remained stable for up to 100 min of hydrogen evolution. Detailed studies on the doping and geometrical structures of the resulting hydrogen evolution cells suggest that both the n^+pp^+ doping and thickness of nanostructures are keys to the enhancement of the hydrogen evolution efficiency. The results obtained in this work show that these silicon nanomaterials can be used for high-performance water-splitting system applications.

Introduction

Energy harvesting directly from sunlight has been a desirable approach toward producing clean energy with minimal environmental impact.[1–3] Conversion of solar energy by photoelectrolysis of water using semiconductors and then subsequently storing the hydrogen in simple molecular form is a highly desirable approach to solve the energy challenge.[4–9] To accomplish the efficient photoelectrolysis of water, the choice of suitable photoelectrode materials is of high importance. The properties of the photoelectrode, such as optical absorption, carrier transportation, and chemical stability, determine the performance of the photoelectrochemical cell.[5–7,9,10] Among the various photoelectrode materials, silicon is an attractive candidate for a photocathode because it possesses both a suitable band gap for efficient sunlight absorption as well as an appropriate position of the conduction band with respect to the electrochemical potential of water reduction.[5,10,11] The main challenge in developing Si-based photocathode materials is to simultaneously achieve high light absorption and efficient charge carrier collection. Recently, the utilization of micro- and nanostructured Si electrodes has attracted attention for solar energy conversion.[7,9,10,12–14] Compared to a planar electrode with the same direction of light absorption and charge carrier collection, the use of nanostructured electrodes allows the directions of light absorption and charge carrier collection to be decoupled while still offering the potential for high energy conversion efficiency.[15,16] Moreover, the nanostructured electrode can significantly increase light absorption by increasing optical path length.[17–20] Thus, the preparation of Si nanostructures of high aspect ratio and high areal density over a large area can be a breakthrough for a realizing a high-performance photoelectrochemical water splitting system.

In this study, we developed precisely controlled, Si nanomaterials (nanomesh and nanowires) of ultra-high aspect ratio on a wafer scale by using the combination of block copolymer lithography and metal-assisted etching. Block copolymer lithography is an emerging approach that provides a variety of periodic nanoscale morphologies having feature sizes ranging from 5 to 50 nm.[21–24] Unlike other nanopatterning techniques such as focused electron-beam lithography[25] or scanning probe lithography,[26] block copolymer lithography provides a parallel patterning process, thereby enabling easy scale-up. In the metal-assisted Si etching method, a thin layer of noble metal on the surface of the Si substrate catalyzes the etching of Si in a mixed solution containing HF and H_2O_2, resulting in parallel pores or columnar structures on the (100) Si substrate.[12,13,27–29] Metal-assisted Si etching is a simple, fast, low-cost and easily scaled-up technique, and various approaches have been derived previously to fabricate Si-based nanostructures.[12,13,29]

[a] Dr. D. H. Lee, Dr. J. Y. Kwon
Department of Materials Science and Engineering
University of Michigan
Ann Arbor, MI (USA)
E-mail: duckhyun.lee@umich.edu

[b] S. P. R. Kobaku
Department of Macromolecular Science & Engineering
University of Michigan
Ann Arbor, MI (USA)

[c] Dr. Y.-R. Hong
Silicium Energy
Sunnyvale, CA (USA)

Supporting information for this article is available on the WWW under http://dx.doi.org/10.1002/ente.201402074.

Results and Discussion

A schematic illustration of the fabrication processes of the Si nanomesh is shown in Figure 1a. The polystyrene (PS) nanoporous template was prepared by self-assembly of a block copolymer spin-coated onto a p-Si wafer. The Au catalytic thin film (20 nm) was deposited onto the PS nanoporous template and the subsequent lift-off process produced hexagonally packed Au catalytic nanoparticles over the entire p-Si substrate surface (Figure 1b). The average diameter and pitch of the Au nanoparticles were 20 nm and 34 nm, respectively. The prepared substrate was dipped into the 6 M HF/0.6 M H_2O_2 aqueous solution for metal-assisted etching.[27,28] Upon etching, holes were generated due to the preferential reduction of the oxidant on the surface of the Au nanoparticles, and the holes diffused through the Au nanoparticles, injecting into the Si substrate. The Si was oxidized by the injected holes and dissolved at the Si/Au nanoparticles interface by HF. This process enabled the etching of the p-Si substrate downward and led to vertically aligned uniform nanopores within the Si substrate.[27,28] The resulting Si nanomesh had hexagonally packed and very uniform nanopores over the p-Si substrate surface with a nanopore diameter of 24 nm (Figure 1c). The pitch of the nanopores and the thinnest width between the nanopores within the p-Si nanomesh were 34 nm and 10 nm, respectively. The etched nanopores ran straight down, parallel to the normal direction of Si surface (Figure 1d); after 10 min of etching, the Au nanoparticles

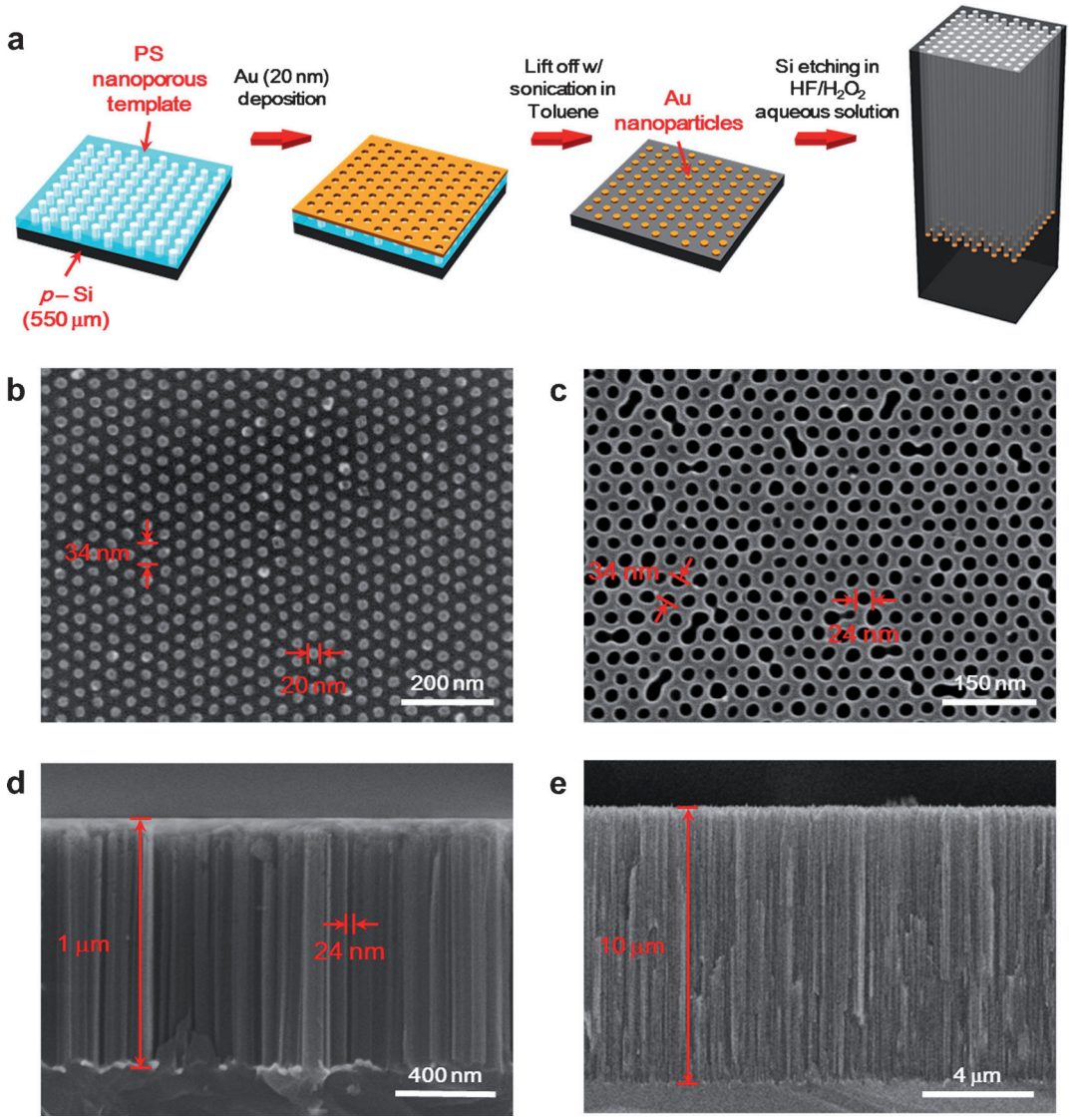

Figure 1. a) Schematic illustration of the Si nanomesh fabrication process. b) Plan-view SEM image of the catalytic Au nanoparticles after lift-off process. The diameter and pitch of the hexagonally packed Au nanoparticles were 20 nm and 34 nm, respectively. c) Plan-view SEM image of the Si nanomesh after 20 s of metal-assisted etching. The image shows the hexagonal packing of the etched nanopores. The diameter and pitch of the nanopores within the nanomesh were 24 nm and 34 nm, respectively. d) and e) Cross-sectional SEM images of Si nanomesh after 1 min. (d) and 10 min (e) of Au-assisted etching. These images show that Si substrate is etched vertically and the diameter of the etched nanopores (24 nm) was maintained uniformly all along the etching direction. The 10 min of metal-assisted etching produced a 10 μm long nanopores array, which resulted in an aspect ratio of 420.

etched nanopores approximately 10 μm deep into the Si substrate (Figure 1e, also see Supporting Information Figure S1).

All the process steps for the preparation of the Si nanowires are similar to those of Si nanomesh (Figure 2a). A thin Cr layer (20 nm) was deposited onto to the PS nanoporous template and the PS template was lifted off to prepare the hexagonally packed uniform Cr nanoparticles with high areal density over the p-Si substrate surface (see Supporting Information, Figure S2a). The hexagonal pattern of Cr nanoparticles was used as a mask for Au-assisted etching of the Si substrate. Before the deposition of the Au thin film, the p-Si substrate with Cr nanoparticles was slightly etched (15 nm) using reactive-ion etching (Figure 2b) to prevent the formation of a continuous Au layer. A thin Au film (8 nm) was deposited onto to the wafer, which provides a honeycomb-structured Au film in contact with the Si surface, and the rest of the Au film is left on top of the Cr nanoparticles (see Supporting Information, Figure S2b). The prepared substrate was dipped into the 6 M HF/0.6 M H_2O_2 aqueous solution, and the thin Au film etched the Si downward leading to a vertically aligned uniform Si nanowire array over the entire substrate surface. For the fabrication of vertically aligned Si nanowires, it is critical to have a high density of Cr nanoparticles as the etching mask. The low density of Cr nanoparticles resulted in non-uniform Si etching, which eventually would lead to the collapse of the nanowires (see Supporting Information, Figure S2c). After 25 min of etching, the vertically aligned uniform Si nanowire array were prepared with an approximate length of 25 μm (see Supporting Information, Figure S1). After drying the Si nanowire array, all of the Si nanowires remained separate (Figure 2c). The diameters of the prepared Si nanowires were very uniform, and the mean diameter of Si nanowire was 20 nm on top and 22 nm on bottom (see Supporting Information, Figure S3a).

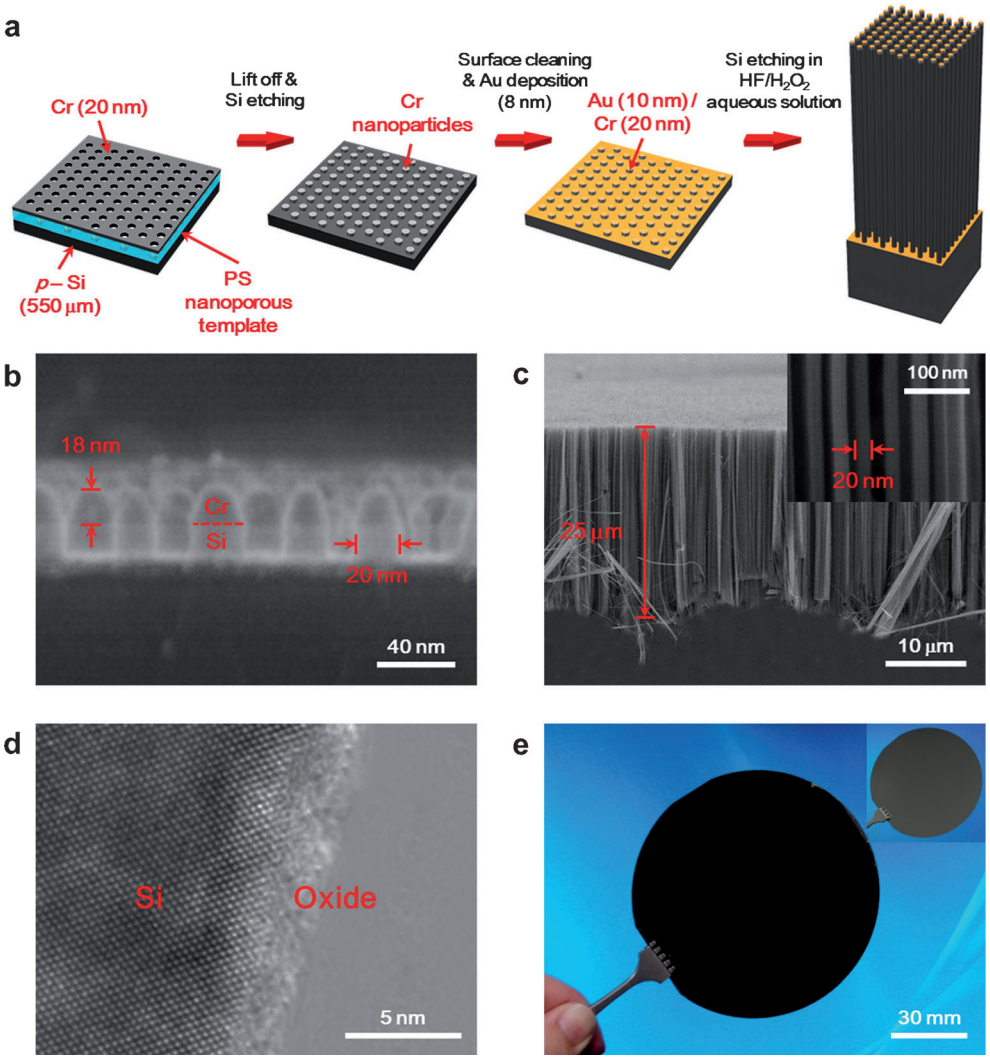

Figure 2. a) Schematic illustration of the Si nanowire array fabrication process. b) Cross-sectional SEM image of the Si nanopillars (height ≈ 15 nm) with Cr nanoparticles on top of the pillars obtained after lift-off and the Si etching step. c) Cross-sectional SEM image of the prepared Si nanowire array after 25 min of Au-assisted etching. The diameter and the length of the Si nanowire were 20 nm and 25 μm, respectively, which resulted in an aspect ratio of 1250. The inset is a high-magnification SEM image of the Si-nanowire array showing that the nanowires remain separated. d) High-resolution TEM image of a segment of a Si nanowire. The roughness at the interface between the crystalline silicon and the amorphous native oxide is observed. e) Optical image of Si nanowire array over an entire 4-inch Si wafer. The inset image shows a bulk 4-inch Si wafer. The dark appearance of the Si wafer with nanowire array as compared to the bulk Si wafer indicates that the Si nanowire array surface is non-reflective due to light scattering by the Si nanowire array.

The TEM image of the Si nanowires (Figure 2d) indicates the formation of a native oxide (≈3 nm thickness) around the single-crystalline Si nanowire lattice. The surfaces of the Si nanowires were very rough (see Supporting Information, Figure S3b), which may be attributed to the randomness of the lateral oxidation and etching in the etching solution.[29] As the all the steps involved in the fabrication process, (the self-assembly of nanotemplates, Au catalyst deposition, and metal-assisted etching) entail parallel processing, this approach can be readily scaled up to the preparation of a large-scale photoelectrochemical hydrogen evolution system. Figure 2e shows the Si nanowire array prepared on an entire 4-inch (1 inch = 2.54 cm) wafer. The dark appearance of the wafer

with the Si nanowire array in comparison to that of bulk Si wafer indicates that the Si nanowire array wafer is non-reflective due to light scattering by the nanowire array, and the rough surface may additionally increase the light absorption.

For the photoelectrochemical hydrogen evolution measurement of the prepared Si nanomesh and Si nanowire substrates, they were doped with phosphorous on the nanostructured side and boron on the other side. This process yields a n^+pp^+ doping structure, which can efficiently separate the charge carriers excited upon light illumination.[8,10,30] Also we deposited a discontinuous layer of Pt electrocatalyst to accelerate the hydrogen evolution reaction while maintaining reasonable photovoltages.[6,10,31] Though there are multiple Pt deposition techniques, we used electroless deposition for its simplicity and low cost. The samples prepared in this way were immersed in an aqueous solution containing 0.1 mM $Na_2PtCl_6{\cdot}6H_2O$ and 0.5 M HF for 10 min at room temperature (see Supporting Information, Figure S4), and connected with metal wire for measurements.

Figure 3a shows the representative current density vs. potential J–E measurement curves under 70 mW cm^{-2} illumination using a tungsten–halogen white light source for three different cells: (1) Pt/n^+pp^+ plane Si cell, (2) Pt/n^+pp^+ 1.1 μm thick Si nanomesh cell, and (3) Pt/n^+pp^+ 1.2 μm long Si nanowire cell measured in aqueous 0.5 M K_2SO_4 solution. The solution was adjusted to pH 1 with H_2SO_4, and the potential was measured by sweeping from positive to negative potentials with a scan rate of 50 mV s^{-1}. The saturated current density (J_{sat}) at −0.8 V vs. reversible hydrogen electrode (RHE) for the plane Si cell, Si nanomesh cell, and Si nanowire cell were measured to be 3.9, 12.6, and 27.4 mA cm^{-2}, respectively. Thus the Si nanomesh and Si nanowire structures increased the photoelectrochemical hydrogen evolution efficiency by over 200% and 570%, respectively, over their bulk counterparts. The current density (J) measured in the dark remains approximately zero over the entire potential range, which indicates that the currents are generated from the light illumination. The photocurrent onset potentials (E_{onset}) were defined as the potential at which the photocurrent and dark current merged in J^2 vs V plots; and E_{onset} was approximately 0.25 V for all three samples and changed negligibly. The significant increase of J may be attributed to following mechanisms: (1) the absorbance enhancement caused by the light scattering in the Si nanomesh and Si nanowire array,[17–20] (2) effective separation of the photogenerated charge carriers achieved along the transverse direction of the nanostructures due to the drastically reduced transport distance of the minority carriers,[15,16] and (3) the nanostructured Si substrates possess a large surface area that greatly enhances water splitting as compared to its smooth bulk counterpart.[5]

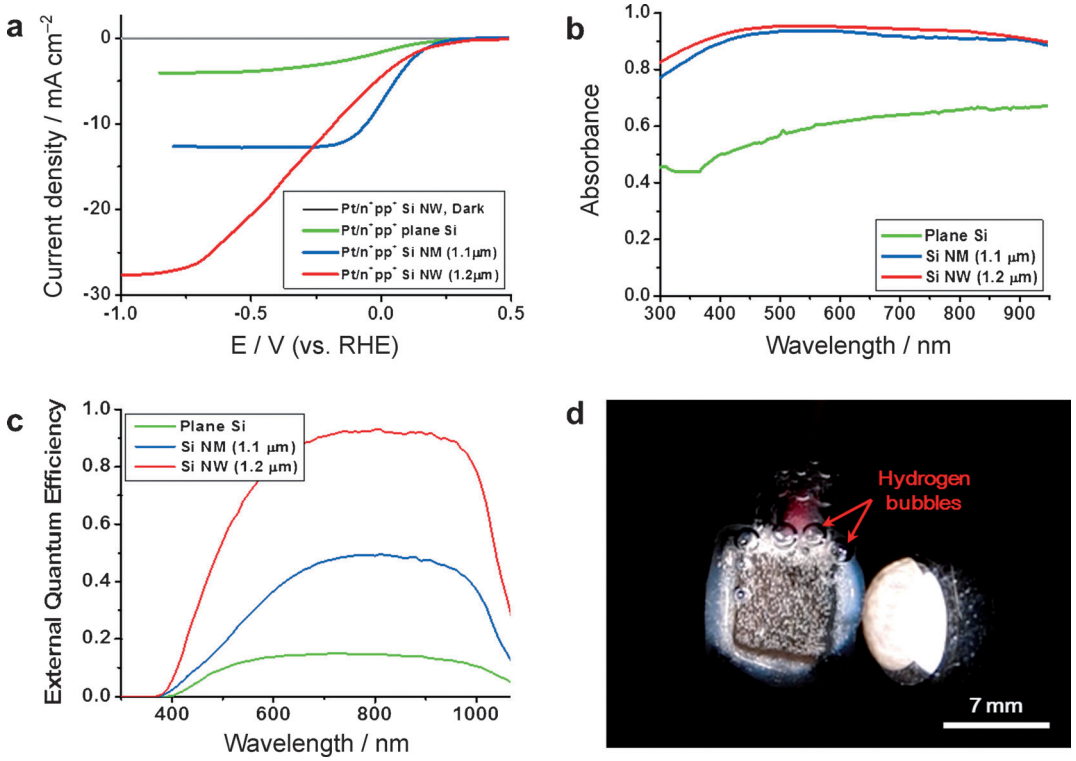

Figure 3. a) Representative current density vs. potential (J–E) curves of the bare p-Si (black), 1.1 μm thick Pt/n^+pp^+ Si nanomesh (blue), and 1.2 μm long Pt/n^+pp^+ Si nanowire (red) cells measured under a light intensity of 70 mW cm^{-2} in aqueous 0.5 M K_2SO_4 solution adjusted to pH 1 with H_2SO_4 (50 mV s^{-1}, single sweep from positive to negative potentials). b) and c) Absorbance spectra (b) and external quantum efficiency spectra (c) for bare Si (black), 1.1 μm thick Si nanomesh (blue), and 1.2 μm long Si nanowire (red). d) Optical image of a normal Pt/n^+pp^+ silicon nanowire array electrode evolving hydrogen at −0.8 V vs. RHE under 70 mW cm^{-2} illumination. Many small bubbles were nucleated on the Si nanowire surface, and further coalesced into large individual bubbles.

To better elucidate the effects of Si nanomesh and Si nanowire structures on the absorbance (A) of our photoelectrochemical hydrogen evolution cells, we measured the reflectance (R) as a function of wavelength in the range of 300–950 nm for the bare Si cell, 1.1 μm thick Si nanomesh cell, and 1.2 μm long Si nanowire cell. Figure 3b shows the calculated absorbance curves for the three cells. The absorbance was calculated by subtracting the reflectance values from unity ($A=1-R$) assuming the transmittance through 550 μm of Si for wavelengths lower than 950 nm is negligible.[20] It is clear (Figure 3b) that the Si nanomesh and Si nanowires dramatically enhanced the optical absorptivity to approximately 95% over a broad range of wavelength from visible to near IR. We also performed external quantum efficiency measurements in the visible and near-IR wavelengths for the three cells. Figure 3c shows the quantum efficiency curves for plane Si (black), the 1.1 μm thick Si nanomesh cell (blue), and the 1.2 μm long Si nanowire cell (red). At a wavelength of approximately 800 nm, the plane Si cell exhibits approximately 15% quantum efficiency, whereas the quantum efficiency values for the Si nanomesh and Si nanowires reache 49% and 93%, respectively, in agreement with the significant increase in J_{SC} caused by Si nanostructures (Figure 3a). From the measurement, we can estimate that the Si nanowire converts approximately 98% (27.4 mA cm^{-2}) of the absorbed light to current for hydrogen evolution. Such high conversion rate is primarily due to the reduced transport distance for minority carriers and increased surface area, and it enabled a high hydrogen evolution rate (Figure 3d, also see Supporting Information Movie 1). However, the Si nanomesh only converts approximately 50% (12.6 mA cm^{-2}) of the observed light to current. This limitation may be due to the difficulty in transportation of the evolved hydrogen bubbles within the high-aspect-ratio nanopores of very small diameter (24 nm). The evolved hydrogen bubble can be captured within the nanopores, which decreases the effective surface area for the water reduction reaction.

To maximize the hydrogen evolution efficiency of photoelectodes, the doping structure and the geometrical structure are critical. We conducted detailed cell performance evaluations for five different photoelectrode cells to better understand the contribution of doping structure:[10,30] (1) bare p-Si nanowire cell without Pt deposition, (2) Pt/bare p-Si nanowire cell, (3) Pt/pp$^+$ Si nanowire cell, (4) Pt/n$^+$p Si nanowire cell, and (5) Pt/n$^+$pp$^+$ Si nanowire cell. Here, we maintained the length of the Si nanowires to be 1.2 μm for all the cells. Figure 4a shows the J–E curves for the five different cells under 70 mW cm^{-2} illumination. The bare p-Si nanowires without Pt deposition showed almost negligible current density, whereas the Pt/n$^+$pp$^+$ Si nanowire cell showed the high-

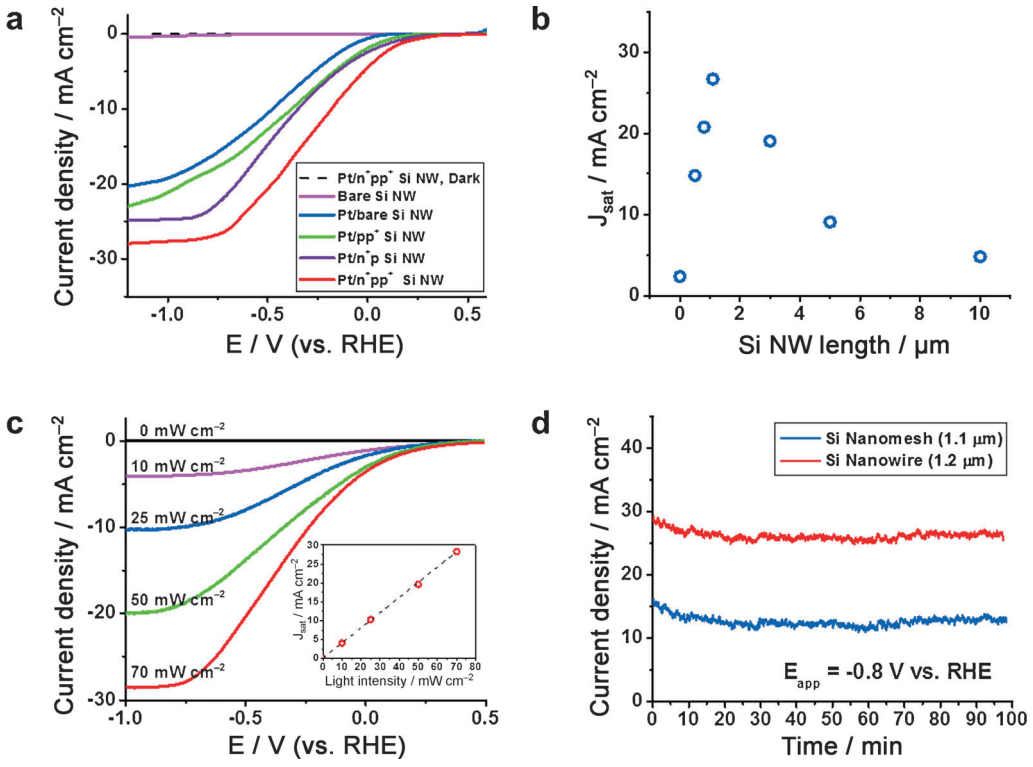

Figure 4. a) *J*--*E* curves of bare p-Si nanowires (magenta), Pt/bare p-Si nanowires (blue), Pt/pp$^+$ Si nanowires (green), Pt/n$^+$p Si nanowire (purple), and Pt/n$^+$pp$^+$ Si nanowires cells under 70 mW cm^{-2} illumination. The average length of the Si nanowires is 1.2 μm. b) Saturated current density (J_{sat}) as a function of the length of Si nanowires measured at −0.8 V vs. RHE. All the electrodes were doped with the n$^+$pp$^+$ structure and 70 mW cm^{-2} of light was illuminated. c) *J*–*E* curves of the Si-nanowires hydrogen evolution electrode at light intensities of 0, 10, 25, 50, and 70 mW cm^{-2}. The inset compares the saturated current density (J_{sat}) at $E=-0.8$ V vs. RHE. d) Long-term current density (J) measurement of the 1.1 μm Pt/n$^+$pp$^+$ Si nanomesh (blue) and the 1.2 mm Pt/n$^+$pp$^+$ Si nanowires (red) as a function of time measured during the hydrogen evolution at −0.8 V vs. RHE. The current initially decreased by approximately 5% in the first 15 min before stabilizing.

est current density (J) and onset potential (E_{onset}). This data clearly show that the Pt catalyst accelerates the hydrogen evolution reaction on the Si nanowire surface, and the combination of n^+ doping on the frontside and p+ doping on the backside efficiently separates the generated charge carriers as well as increases the onset potential of the photoelectrodes. These observations are in agreement with the results obtained from plane Si cells and Si nanomesh cells (see Supporting Information, Figure S5).

The saturated current density (J_{sat}) as a function of Si nanowire length is presented in Figure 4b as measured at −0.8 V vs. RHE under 70 mW cm^{-2} illumination. All of the cells were prepared with the Pt/n$^+$pp$^+$ Si nanowire structure. The data shows that the 1.2 μm long Si nanowire cell leads to the highest enhancement in current density. Interestingly, if the length of Si nanowire was higher than 3 μm, the current density decreased (also see Supporting Information, Figure S6). This behavior may be attributed to the morphology of Pt deposition. The electroless Pt deposition method forms an approximately 1 μm deep, high-density Pt particle layer from the top end of Si nanowires (see Supporting Information, Figure S7). Therefore, if the length of the Si nanowire is approximately longer than 1 μm, the charge carriers generated from the light illumination near the bottom of the Si nanowires need to transfer to the top end of Si nanowire for hydrogen evolution, which may increase the chance of charge recombination.

To better understand the photoelectrochemical behavior of the Pt/n$^+$pp$^+$ Si nanowire photoelectrode, we measured the current density at various light intensities. Figure 4c shows the J–E measurement curves under the light intensity of 0–70 mW cm^{-2}. The inset compares the saturated current density (J_{sat}) at $E = -0.8$ V vs. RHE. as a function of light intensity, and it shows a linear relationship of current density and illumination power, which indicates that the Si nanowire photoelectrode has constant efficiency of charge separation under the condition of sufficient cathodic polarization.[32] We also ran the experiments for 100 min to confirm the stability of the hydrogen evolution with time on the Si nanomesh and Si nanowire electrodes. Figure 4d shows the current density (J) as a function of time measured during the hydrogen evolution at $E = -0.8$ V vs. RHE under 70 mW cm^{-2} illumination. The current densities slightly decreased in the first 15 min, however they produced stable current density and hydrogen evolution for up to 100 min of experimental run time.

Conclusions

The results from this work illustrate the successful fabrication of photoelectrochemical cells based on Si nanomesh and Si nanowire arrays with features as small as 20 nm with high aspect ratio. Thus Si-nanostructured cells were fabricated using scalable manufacturing techniques; they exhibited enhanced optical absorptivity up to 95%, reduced minority carrier transport distance, and extremely high chemical reaction surface area. These structural advantages of the Si nanostructures developed here enabled us to develop highly efficient photoelectrochemical hydrogen evolution cells with long-term stability. Detailed studies on the doping structure and geometrical structure of the Si nanomaterials further elucidated their effects on the overall hydrogen evolution efficiency. The results reported here may provide useful design considerations for developing a highly efficient photoelectrochemical water splitting system and other classes of solar energy conversion systems in the future.

Experimental Section

Nanoporous polymer template preparation

The (100) Si surface was neutrally treated with a random copolymer brush. A thin film (100 nm) of asymmetric block copolymer, polystyrene-block-poly(methyl methacylate) (PS-b-PMMA) that forms cylindrical nanostructures upon annealing (molecular weight: PS/PMMA = 46.1k/21k; PMMA cylinder diameter: 18 nm, pitch distance between neighboring cylinders: 34 nm) was spin-coated onto the wafer surface and annealed at 190 °C for 24 h. After annealing, the substrates were irradiated with ultraviolet light (254 nm) for 30 min, and subsequently rinsed with acetic acid (30 min) and water (5 min) to remove the PMMA cylinder cores. This left a nanoporous polystyrene template over the entire silicon surface.

Fabrication of Si nanomesh electrode

The substrates with polystyrene nanoporous template were treated with CF_4/O_2 plasma (O_2/CF_4 = 20 sccm/20 sccm, 20 mtorr, 50 W, 17 s) to remove the remnant PMMA cylinder cores and etch the Si substrate slightly. The substrates were cleaned with BHF (10 s) and then rinsed with DI water to remove the oxide layer on the exposed Si surface (within the nanopores). A thin Au film (20 nm) was deposited over the PS nanoporous template, and the PS nanoporous template was lifted-off upon sonication in toluene. This lift-off process leaves uniformly sized Au nanoparticles arrayed in a hexagonal lattice defined by the pores of the nanoporous PS template. Thus prepared substrates were dipped into 6 M HF/0.6 M H_2O_2 aqueous solution for 0–10 min for Au catalysed Si etching. After the Au catalysed etching, Au was removed with Au etchant, and rinsed with DI water.

Fabrication of Si nanowire electrode

The substrates with the polystyrene nanoporous template were further treated with oxygen plasma (O_2 40 sccm, 20 mtorr, 50 W, 15 s) to remove any remnant PMMA cylinder cores. The thin film of Cr (20 nm) was deposited over the nanoporous PS template. After the deposition process, the nanoporous PS template was lifted off by sonication in a piranha solution (20 min). This lift-off process leaves uniformly sized Cr nanoparticles arranged in a hexagonal lattice defined by the pores of the nanoporous PS template. This hexagonal lattice of Cr nanoparticles was used an etching mask for the Au-catalyzed Si etching. To prevent the continuous layer of Au film, the exposed Si surface (through the Cr nanoparticle mask) was slightly etched (≈15 nm) by using reactive ion etching (RIE) (SF_6/C_4F_8 = 10 sccm/20 sccm, 100 W/100 W, 5 mtorr, 20 s), and the etched Si surface was cleaned using a piranha solution and BHF for 10 min and 20 s, respectively. Then a thin Au catalyst film (8 nm) was deposited on the

Si surface. The surfaces with the deposited Au catalyst were dipped into a 6 M HF/0.6 M H_2O_2 aqueous solution for 0–20 min. The Au catalyst in contact with the Si surface (defined by the Cr nanoparticle mask) etched the Si vertically through the Cr-nanoparticle etching mask leading to a dense, vertical Si nanowire array. After the metal-assisted etching, the Cr/Au was removed with the Cr/Au etchant and rinsed with DI water.

Platinum deposition

The prepared low-doped (doping concentration: $\approx 10^{15}$ cm^{-3}) p-type silicon nanowire/nanomesh electrodes were doped with with boron at the bottom and phosphorous at the top using solid targets in a tube furnace at 1000 °C for 20 min (doping concentration: $\approx 10^{20}$ cm^{-3}, doping thickness: ≈2 μm). The silicon nanowire/nanomesh was completely doped with phosphorous using this process. Pt deposition on the prepared Si nanomesh/nanowire electrodes was accomplished using a galvanic displacement reaction in which Si is oxidized and Pt is reduced onto the electrode surface. The solution used for Pt deposition contained 0.05–1 mM $Na_2PtCl_6 \cdot 6H_2O$ and 0.5 M HF. The electrodes were immersed in the solution for 10 min at room temperature without stirring of the solution. After Pt deposition, a thin Al film (100 nm) was deposited on the back side of electrodes by using electron-beam evaporation at a base pressure of approximately 2×10^{-6} torr. The Al-deposited electrodes were connected with a metal wire for measurements, and the electrodes were completely sealed with epoxy with the exception of a working area of approximately 0.5 cm^2.

Photoelectrochemical activity measurements

All of the photoelectrochemical measurements were performed in aqueous 0.5 M K_2SO_4 solution, and the solution was adjusted to pH 1 with H_2SO_4. The measurements were performed by using a three-electrode configuration utilizing a Pt wire as a counter electrode and a Ag/AgCl electrode as the reference electrode. The potential was swept from positive to negative potentials with a scan rate of 50 $mV\,s^{-1}$. Data was measured with versa STAT 3 (Princeton Applied Research), and the collected data were shifted on the potential axis so that the potential of the reversible hydrogen electrode (RHE) was zero. During the measurements, the cells were illuminated using a tungsten–halogen lamp with the intensity of 0–70 $W\,cm^{-2}$ at the working electrode, and the light intensity was calibrated by using a Si photodiode.

Absorbance and Quantum efficiency measurement

Absorbance measurements were obtained using an Oriel 150 W Xe arc lamp (Newport) and a quarter-turn single-grating monochromator (Newport). Sample measurements were recorded using chopped illumination (15 Hz), and a quartz beam splitter was used to simultaneously record the light output intensity with a separate Si photodiode (Newport) to adjust for fluctuations in lamp intensity. The wavelength-dependent external quantum yield values were measured at −0.8 V vs. RHE for each device, and the absolute photocurrents were measured using a digital PAR 273 potentiostat. The output current signal was connected to a Stanford Instruments SR830 lock-in amplifier, and the output signals from the lock-in amplifier and the reference Si photodiode were fed into a computer controlled by custom-written LabVIEW software.

Acknowledgements

We acknowledge financial support from the National Science Foundation (grant CBET-1066447), and the Air Force Office of Scientific Research (AFOSR) (grant FA9550-11-1-0017). This work used the Lurie Nanofabrication Facility at the University of Michigan, a member of the National Nanotechnology Infrastructure Network funded by the National Science Foundation.

Keywords: block copolymers · hydrogen production · nanomaterials · photoelectrolysis · silicon

[1] M. S. Dresselhaus, I. L. Thomas, *Nature* **2001**, *414*, 332.
[2] L. Schlapbach, A. Zuttel, *Nature* **2001**, *414*, 353.
[3] A. I. Hochbaum, P. D. Yang, *Chem. Rev.* **2010**, *110*, 527.
[4] M. Grätzel, *Nature* **2001**, *414*, 338.
[5] M. G. Walter, E. L. Warren, J. R. McKone, S. W. Boettcher, Q. X. Mi, E. A. Santori, N. S. Lewis, *Chem. Rev.* **2010**, *110*, 6446.
[6] A. Kudo, Y. Miseki, *Chem. Soc. Rev.* **2009**, *38*, 253.
[7] S. W. Boettcher, J. M. Spurgeon, M. C. Putnam, E. L. Warren, D. B. Turner-Evans, M. D. Kelzenberg, J. R. Maiolo, H. A. Atwater, N. S. Lewis, *Science* **2010**, *327*, 185.
[8] S. Y. Reece, J. A. Hamel, K. Sung, T. D. Jarvi, A. J. Esswein, J. J. H. Pijpers, D. G. Nocera, *Science* **2011**, *334*, 645.
[9] Y. Hou, B. L. Abrams, P. C. Vesborg, M. E. Bjorketun, K. Herbst, L. Bech, A. M. Setti, C. D. Damsgaard, T. Pedersen, O. Hansen, J. Rossmeisl, S. Dahl, J. K. Norskov, I. Chorkendorff, *Nat. Mater.* **2011**, *10*, 434.
[10] S. W. Boettcher, E. L. Warren, M. C. Putnam, E. A. Santori, D. Turner-Evans, M. D. Kelzenberg, M. G. Walter, J. R. McKone, B. S. Brunschwig, H. A. Atwater, N. S. Lewis, *J. Am. Chem. Soc.* **2011**, *133*, 1216.
[11] Q. Ding, F. Meng, C. R. English, M. Caban-Acevedo, M. J. Shearer, D. Liang, A. S. Daniel, R. J. Hamers, S. Jin, *J. Am. Chem. Soc.* **2014**, *136*, 8504.
[12] M. T. Mayer, C. Du, D. Wang, *J. Am. Chem. Soc.* **2012**, *134*, 12406.
[13] X. Li, Y. Xiao, J. H. Bang, D. Lausch, S. Meyer, P. T. Miclea, J. Y. Jung, S. L. Schweizer, J. H. Lee, R. B. Wehrspohn, *Adv. Mater.* **2013**, *25*, 3187.
[14] E. L. Warren, J. R. McKone, H. A. Atwater, H. B. Gray, N. S. Lewis, *Energy Environ. Sci.* **2012**, *5*, 9653.
[15] B. M. Kayes, H. A. Atwater, N. S. Lewis, *J. Appl. Phys.* **2005**, *97*, 114302.
[16] M. J. Price, S. Maldonado, *J. Phys. Chem. C* **2009**, *113*, 11988.
[17] B. Z. Tian, X. L. Zheng, T. J. Kempa, Y. Fang, N. F. Yu, G. H. Yu, J. L. Huang, C. M. Lieber, *Nature* **2007**, *449*, 885.
[18] L. Hu, G. Chen, *Nano Lett.* **2007**, *7*, 3249.
[19] J. Zhu, Z. Yu, G. F. Burkhard, C. M. Hsu, S. T. Connor, Y. Xu, Q. Wang, M. McGehee, S. Fan, Y. Cui, *Nano Lett.* **2009**, *9*, 279.
[20] J. Y. Kwon, D. H. Lee, M. Chitambar, S. Maldonado, A. Tuteja, A. Boukai, *Nano Lett.* **2012**, *12*, 5143.
[21] S. J. Jeong, G. D. Xia, B. H. Kim, D. O. Shin, S. H. Kwon, S. W. Kang, S. O. Kim, *Adv. Mater.* **2008**, *20*, 1898.
[22] D. H. Lee, W. J. Lee, S. O. Kim, *Nano Lett.* **2009**, *9*, 1427.
[23] D. Zschech, D. H. Kim, A. P. Milenin, R. Scholz, R. Hillebrand, C. J. Hawker, T. P. Russell, M. Steinhart, U. Gosele, *Nano Lett.* **2007**, *7*, 1516.
[24] J. Y. Cheng, A. M. Mayes, C. A. Ross, *Nat. Mater.* **2004**, *3*, 823.
[25] E. M. Hicks, S. L. Zou, G. C. Schatz, K. G. Spears, R. P. Van Duyne, L. Gunnarsson, T. Rindzevicius, B. Kasemo, M. Kall, *Nano Lett.* **2005**, *5*, 1065.
[26] S. Y. Chou, P. R. Krauss, P. J. Renstrom, *Science* **1996**, *272*, 85.
[27] Z. P. Huang, N. Geyer, P. Werner, J. de Boor, U. Gosele, *Adv. Mater.* **2011**, *23*, 285.

[28] K. Q. Peng, A. J. Lu, R. Q. Zhang, S. T. Lee, *Adv. Funct. Mater.* **2008**, *18*, 3026.
[29] A. I. Hochbaum, R. K. Chen, R. D. Delgado, W. J. Liang, E. C. Garnett, M. Najarian, A. Majumdar, P. D. Yang, *Nature* **2008**, *451*, 163.
[30] J. J. H. Pijpers, M. T. Winkler, Y. Surendranath, T. Buonassisi, D. G. Nocera, *Proc. Natl. Acad. Sci. USA* **2011**, *108*, 10056.
[31] I. Lombardi, S. Marchionna, G. Zangari, S. Pizzini, *Langmuir* **2007**, *23*, 12413.
[32] F. Amano, D. Li, B. Ohtani, *Chem. Commun.* **2010**, *46*, 2769.

Received: July 4, 2014
Revised: September 2, 2014
Published online on September 18, 2014

